Morphodynamic modeling of a large inside sand bar and its dextral morphology in a convergent estuary: Qiantang Estuary, China

Xie, Dongfeng; Gao, Shu; Wang, Zhengbing ; Pan, Cunhong; Wu, Xiuguang; Wang, Qiushun

DOI
10.1002/2017JF004293

Publication date
2017

Document Version
Final published version

Published in
Journal of Geophysical Research: Earth Surface

AGU PUBLICATIONS

JGR

Journal of Geophysical Research: Earth Surface

RESEARCH ARTICLE
10.1002/2017JF004293

Key Points:
- The relative strengths of river flow and tidal currents determine the location of the large bar in Qiantang Estuary
- River discharge variations are responsible for the interannual and seasonal fluctuations of the bar morphology
- Coriolis effect is responsible for the dextral morphological patterns in this estuary

Correspondence to:
D. Xie,
dongfeng.xie@hotmail.com

Citation:
Xie, D., S. Gao, Z. B. Wang, C. Pan, X. Wu, and Q. Wang (2017), Morphodynamic modeling of a large inside sandbar and its dextral morphology in a convergent estuary: Qiantang Estuary, China, *J. Geophys. Res. Earth Surf.*, *122*, doi:10.1002/2017JF004293.

Received 21 MAR 2017
Accepted 16 JUL 2017
Accepted article online 10 AUG 2017

Morphodynamic modeling of a large inside sandbar and its dextral morphology in a convergent estuary: Qiantang Estuary, China

Dongfeng Xie[1], Shu Gao[2], Zheng Bing Wang[3,4], Cunhong Pan[1], Xiuguang Wu[1], and Qiushun Wang[1]

[1]Zhejiang Institute of Hydraulics and Estuary, Hangzhou, China, [2]State Key Laboratory for Estuarine and Coastal Research, East China Normal University, Shanghai, China, [3]Faculty of Civil Engineering and Geosciences, Delft University of Technology, Delft, Netherlands, [4]Deltares, Delft, Netherlands

Abstract We investigate the evolution of a large-scale sand body, a unique type of sandbars in a convergent estuary. Specifically, we analyze and simulate the sand deposition system (defined as an inside bar) in the Qiantang Estuary (QE) in China. The deposit is 130 km long and up to 10 m thick and is characterized by a dextral morphology in the lower QE. Numerical simulation is carried out using an idealized horizontal 2-D morphodynamic model mimicking the present QE settings. Our results indicate that the morphological evolution is controlled by the combination of river discharge and tides. The seasonal and interannual cycles of river discharges play a major role on the inside bar evolution. The bar is eroding during high river discharge periods, but accretion prevails during low river discharge periods. Meanwhile, the highest part of the sand body can move downstream or upstream by several kilometers, modifying the seasonal sediment exchange patterns. We also show that the Coriolis force plays an important role on the dextral morphology patterns in wide, convergent estuaries. It induces a significant lateral water level difference and a large-scale gyre of residual sediment transport. Subsequently, the seaward tail of the inside bar shifts southward to help create a condition for the development of tidal flats in the lower reach of the estuary. The lateral bed level differences induced by Coriolis force are up to several meters. Coriolis effects also modify the behavior of flood and ebb tidal channels.

1. Introduction

Estuaries are the connections between the land and the sea, where rivers meet the tides [*Dyer*, 1986; *Carter and Woodroffe*, 1994; *Savenije*, 2005]. Quite often, they are subjected to intense human activities, allowing the development of harbors, shipping channels, and recreational facilities. The intertidal areas are important feeding and breeding grounds for a variety of species and thus of great ecological importance. In estuaries, large sand bodies in various forms are often observed to be one of the key morphological features. They are accretional features with different configurations and spatial scales, which are determined by the interactions of hydrodynamics, including river discharges, tides, waves, and sediment transport related to sediment supply, sediment composition, and other physical processes like saltwater intrusion and biogeochemistry [e.g., *Carter and Woodroffe*, 1994; *Leuven et al*., 2016]. From the viewpoint of coastal management, it is of major importance to gain insight into the morphological behavior of such deposits and assess the effects of various natural changes and human interventions.

According to their locations in estuaries, the sand bodies have different categories. Estuarine mouth bars are located at the entrance to the embayment, with a transverse morphology in relation to the dominant flow direction, and ebb tidal deltas are located outside the entrance, associated with tidal inlet systems [e.g., *Carter and Woodroffe*, 1994; *Geleynse et al*., 2011; *Nardin et al*., 2013]. In some estuaries, sand deposits are widely distributed within the estuarine embayment, forming a first-order morphological unit. In literature, these types of sand deposits have been defined as estuarine "sandbars" [e.g., *Chien et al*., 1964]. In order to avoid any misunderstanding of the term "sandbar," in the present contribution, such features will be referred to as "inside bars." As far as the inside bar is concerned, the processes of river-tide interaction and its influences on the sand body are only poorly understood, although a number of observations have been made [e.g., *Chien et al*., 1964; *Harris*, 1988; *Dalrymple et al*., 1990; *Kunte et al*., 2005; *Yu et al*., 2012]. Thus, a detailed study on the inside bar will be beneficial to the enhancement of our ability to predict the future dynamics of

estuarine morphodynamics resulting from natural and/or human activity factors or to interpret the deposits formed in the past.

The inside bar in the upper and middle reaches of the Qiantang Estuary (QE), China, represents a typical example. It starts at about 80 km from the mouth, extends by about 130 km along the longitudinal bed profile, and has a height of 10 m above the baseline at the top of the deposit (Figure 1). Apparently, this system is much larger than most linear bars in estuarine environments, normally in the order of 10^{-4}–10^{1} km [*Leuven et al*., 2016]. In addition, the large inside bar in QE is different from flood delta which is usually observed in tidal basins and dominated by flood tidal currents [e.g., *O'Brien*, 1969; *Zhou et al*., 2014]. Its overwhelming spatial scale results in a series of problems in terms of saltwater intrusion, flood defense, navigations, water diversions, and estuarine regulations. Based on past bathymetric and hydrological data, *Chien et al*. [1964] and *Chen et al*. [1964] analyzed the morphological evolution pattern of the inside bar, proposing that the sediment source is mainly from the adjacent Changjiang Estuary, and the inside bar formation is due to the small ratio of the river and tidal discharges. Recently, *Yu et al*. [2012] studied the sand body morphodynamics in QE using a 2-D long-term morphodynamic model based on noncohesive sediment transport. Their results revealed that the sand body evolution is related to the river discharge, sediment grain size, and gradation, the planar shape of the estuary. However, the role of the seasonal river discharge on the shorter time scale morphological evolution was not taken into account. Furthermore, in their model they were unable to define the lateral morphological development due to the coarse model grid (i.e., six transversal grids for about 100 km width).

Long-term morphodynamic modeling provides a powerful tool to investigate the formation and the underlying physical mechanisms of morphological patterns observed in the real world [e.g., *Wang et al*., 1995; *Lanzoni and Seminara*, 2002; *Van der Wegen and Roelvink*, 2008; *Geleynse et al*., 2011; *Nardin et al*., 2013]. Most of the previous models neglected the river discharge, assuming that it was much smaller than the prevailing tidal discharge. However, although tides dominate over most of an estuary, river discharge and the associated sediment supply pattern may play an important role at the landward end where smaller channel cross sections and tidal prisms prevail [*Perillo*, 1995]. River flows attenuate tidal currents through enhanced tidal friction and constrain landward saltwater intrusion by enlarging ebb currents [*Godin*, 1985; *Savenije*, 2005]. Considerable morphological changes in estuarine environments may take place due to high river discharges. *Cooper* [1993], *Shaw and Mohrig* [2014], *Bravard et al*. [2014], and *Wang et al*. [2014] documented the importance of high river discharge, in particular, the seasonal high flow with high sediment influx in driving fluvial and estuarine morphodynamics. Recently, *Guo et al*. [2014] explored the impact of seasonal river discharge and river-borne sediment supply variations on long-term estuarine morphodynamic behavior by means of a 1-D morphodynamic model. Yet thus far, few studies have been reported on the role of seasonal river flow on the estuarine inside bar system.

The Coriolis force deflects the bulk of a gravity current to the right in the Northern Hemisphere (dextral diversion) [e.g., *Schramkowski and de Swart*, 2002; *Van der Vegt*, 2006; *Li et al*., 2011] and leads to secondary circulations in estuarine waters. Gradual propagation in association with dextral diversion affects the sediment transport pathways and the delta-coastal morphology in the Northern Hemisphere [e.g., *Li et al*., 2011]. In estuarine environments, such dextral morphological extension can be identified worldwide, e.g., the Elbe, Ganges-Brahmaputra, Nile, and Chesapeake Bay [*Goodbred and Kuehl*, 2000; *Woodroffe et al*., 2006; *Huijts et al*., 2009; *Li et al*., 2011; *Bravard et al*., 2014]. Based on past charts and geological surveys, the morphological developments of the three largest estuaries in China, namely, the Changjiang, Yellow, and Pearl, as well as QE, are characterized by the dextral morphology and thought to be related to the Coriolis force [*Chen et al*., 1990, 1988; *Li*, 2007]. *Jiang* [1987] analyzed the tidal range difference (more than 1 m) between the two banks of Hangzhou Bay and attributed the notable difference to the Coriolis effects. *Jin and Shen* [1993] proposed an analytical method for the water level difference induced by the Coriolis force in the Changjiang Estuary. Using hydrological survey data from several stations in CE, *Li et al*. [2011] proved that the Coriolis effect on the tidal currents and sediment fluxes is significant and argued that it is responsible for the dextral morphology. *Schramkowski and de Swart* [2002] analyzed the role of Coriolis force on the lateral geomorphological development in straight tidal channels using a three-dimensional morphodynamic model and found that the sediment-dispersive flux generated by the Coriolis force is much larger than the flux due to gravitational downslope effects. *Van der Vegt* [2006] revealed that Coriolis effects can weakly influence the ebb tidal delta

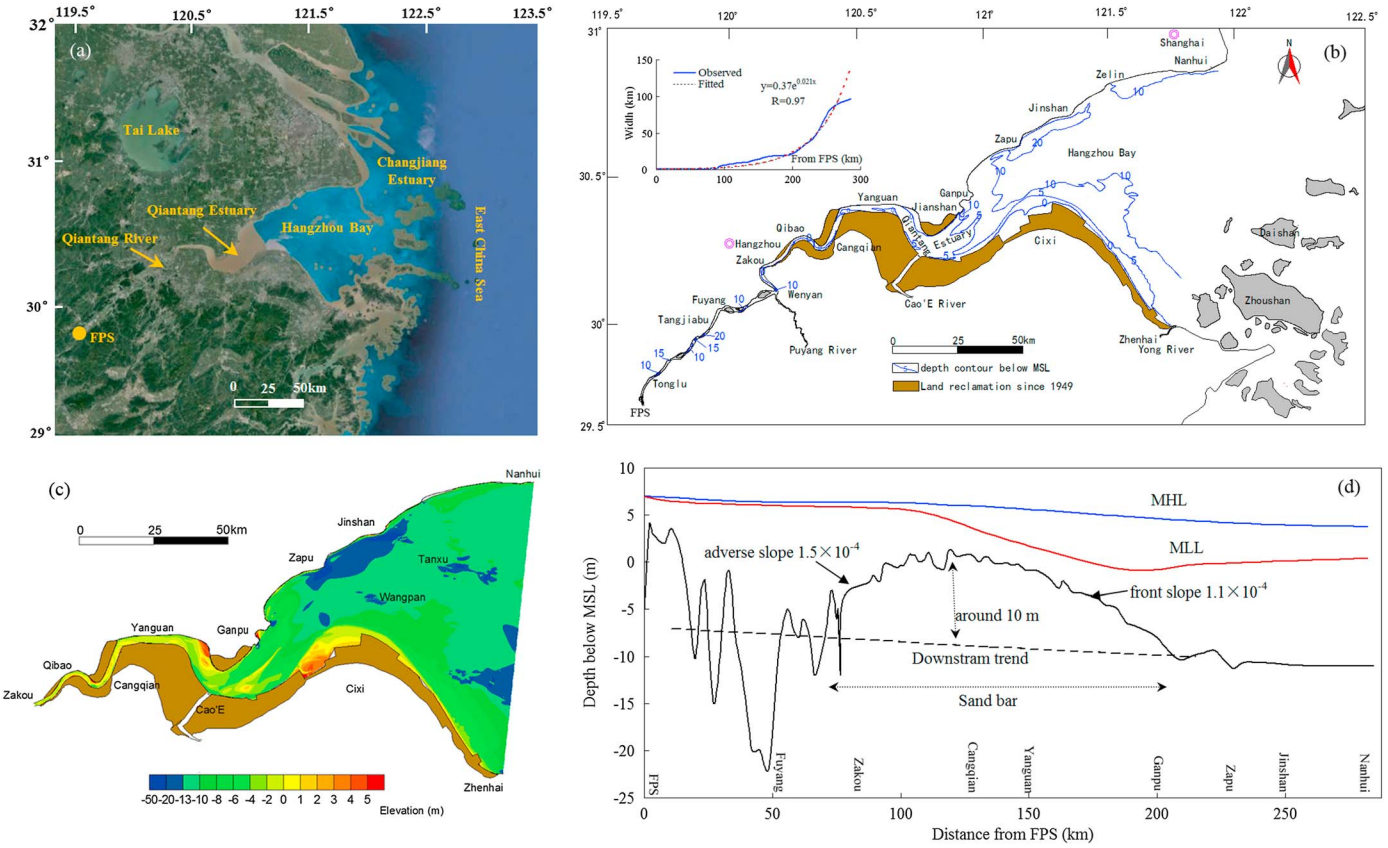

Figure 1. (a) Location of Qiantang Estuary, (b) the planar bathymetry, (c) 2-D bathymetry downstream of Zakou, and (d) the lateral-averaged longitudinal bathymetries and the mean high and low tidal levels along the estuary. The lateral-averaged bed elevation in the longitudinal profile is obtained from the survey data in 2014, as shown in Figure 1c. The width in the upper left panel of Figure 1b is measured from the present estuary, without regard for the reclaimed area. FSP in the panels denotes the Fuchun power station. The image in Figure 1a is from Google Earth. Bathymetric data in Figures 1b–1d were collected from Zhejiang Surveying Institute of Estuary and Coast, China (ZSIEC).

development in tidal inlet systems. *Huijts et al.* [2009] reasoned that the Coriolis force modified the circulating residual flows that are landward to the right and seaward to the left in Chesapeake Bay. It is valuable to explore quantitatively the role of Coriolis force on the large-scale morphodynamic evolution of convergent estuaries and the underlying physical mechanisms based on a process-based model.

The purpose of this study is to (1) reproduce the formation of the inside bar of QE, using an idealized physically based numerical model; (2) explore the influence of the seasonal and interannual variations of the river discharges on the inside bar morphodynamics; and (3) test the significance of the Coriolis force on the dextral morphological patterns in the estuary.

2. The Qiantang Estuary

2.1. Physical Geography

The Qiantang Estuary is one of the largest estuaries located on the coast of East China Sea, immediately south of the Changjiang Estuary (CE) (Figure 1a). The upper part of QE extends in the SW-NE direction, and the lower part is in the west-east direction. It covers a catchment area of around 56,000 km^2 [*Han et al.*, 2003]. The length of QE is 282 km, and the width converges exponentially from 98.5 km at the mouth to less than 1 km at the landward end (the upper left panel in Figure 1b).

According to the hydrodynamic controls, the estuary can be divided into three reaches [*Chen et al.*, 1990; *Han et al.*, 2003; *Fan et al.*, 2014]. The upper reach of 87 km in length, from the Fuchun Power Station (FPS) to Zakou, is characterized by river discharge, and the bathymetry is basically stable. The middle reach from Zakou to Ganpu, with a length of 108 km, is controlled by a combination of river flow and tidal currents.

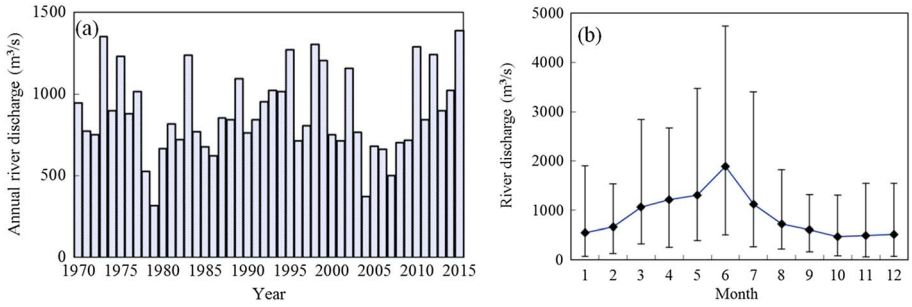

Figure 2. (a) Annually and (b) monthly averaged discharges of Qiantang River. The error bars in Figure 2b reflect the monthly maximum and minimum discharges. The data were collected from Hydrology Bureau of Zhejiang Province, China (HBZPC).

The lower reach of 85 km length downward from Ganpu, also well known as Hangzhou Bay, is controlled by tidal currents.

The most remarkable morphological feature in QE is the presence of the inside bar, a large subaqueous body (Figure 1). It extends from Zapu at the middle Hangzhou Bay to Tangjiabu in the upper reach. The bed level at Zapu is about 10 m below mean sea level and rises gradually upstream to above 0 m, with its top part swinging repeatedly within the Qibao-Cangqian section. The front slope from Zapu to the top is about 1.1×10^{-4}, and the slope from the top to Tangjiabu is about 1.5×10^{-4}.

The southern bank of the estuary is flanked by a large area of tidal flats, downstream from Zakou to the mouth (Figures 1b and 1d). Historically, the tidal flats advanced rapidly, with a propagation rate of the southern flat being up to 10–70 m/yr [*Chen et al*., 1990; *Han et al*., 2003]. The northern bank of Hangzhou Bay had been eroding continuously since the formation of the bay in about 3000 years B.C.; as a result, shoreline retreat occurred until the seawall was built after the fifteenth century [*Chen et al*., 1990]. In the present-day northern Hangzhou Bay, a large tidal channel system is developed upstream of Jinshan, with the length and width of 20 m depth contour up to 20 km and 5 km, respectively. Downstream from Jinshan, there is a large subaqueous plain with an average depth of around 11 m. Overall, the lower QE is characterized by the dextral morphological patterns; namely, the southern and northern parts tend to be accretional and erosional, respectively.

The tides in QE come from the East China Sea. It is mainly composed of semidiurnal M_2 constituent [*Editorial Committee for Chinese Harbors and Embayments* (*ECCHE*), 1992; *Han et al*., 2003]. The mean tidal range is about 3.2 m and 1.8 m at the north and south mouth locations, respectively [*ECCHE*, 1992]. The tidal waves are seriously deformed upstream due to the width convergence and the bathymetric lift upward and evolve into the world famous Qiantang bore. The tidal range increases landward and reaches its maximum of up to 9 m at Ganpu. Before the construction and operation of FPS in 1977, the tidal wave could trace to about 5 km upstream of FPS during spring tides. After 1977, the tidal limit shifted down to FPS [*Han et al*., 2003]. Wind waves are weak in this area, with the annually averaged wave height of 0.5 m at the Tanxu station (water depth of about 9 m) of the lower QE [*ECCHE*, 1992].

The annually averaged discharge of the Qiantang River is 952 m^3/s. On the interannual time scales, the annually averaged discharges fluctuate between 319 and 1390 m^3/s. Continuous wet and dry years have been recorded (Figure 2a). Due to the seasonal monsoon, the low discharge occurs from August to March in the following year and the high discharge occurs from April to July, with the peak in June, being 1893 m^3/s (Figure 2b). During high flow season, the flood peaks can be more than 10,000 m^3/s, with the daily maximum being 12,787 m^3/s since 1977.

Sediment supply from Qiantang River is only 6 Mt/yr [*Han et al*., 2003]. Sediment in QE is mainly from the seaside. Parts of the large sediment load from the Changjiang River (used to be 500 Mt/yr) disperse southerly and enter QE by tidal currents [*Su and Wang*, 1989; *Chen et al*., 1990]. With the large sediment input from CE, the QE has been always deposited and the annual sediment accumulation can be up to 130×10^6 m^3 [*Han et al*., 2003]. Sediment in QE is mainly composed of fine-sorted silt and clay. The median grain size is between 20 and 90 μm, with those of 20 to 40 μm dominating [*Chen et al*., 1990; *Han et al*., 2003; *Fan et al*., 2014].

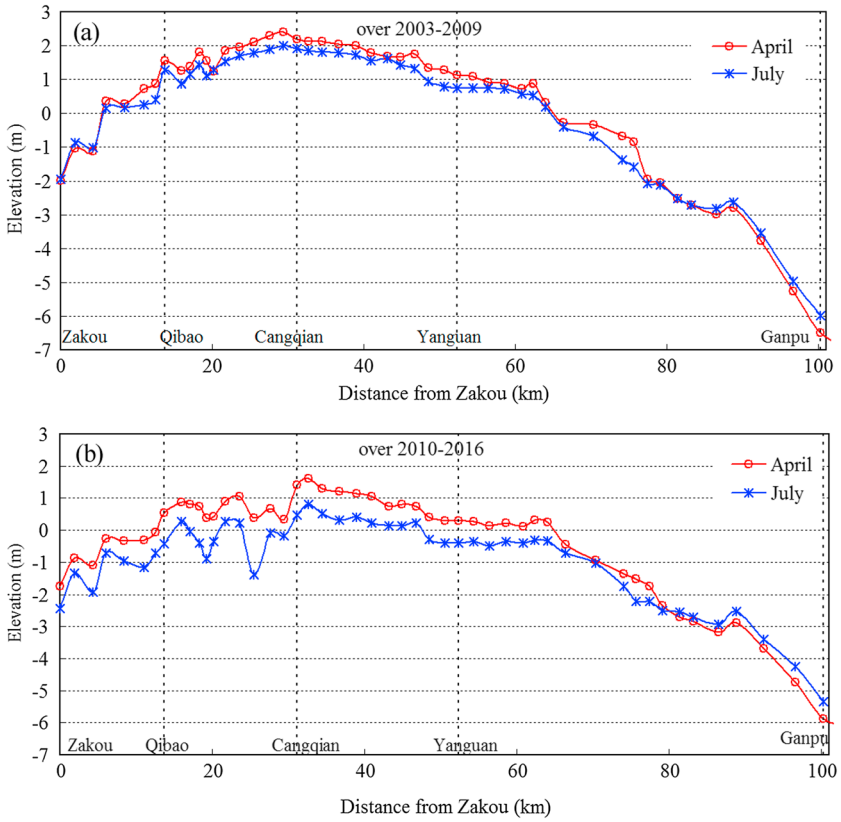

Figure 3. The lateral-averaged longitudinal profile of the estuarine reach in April and July over years. (a) During the continuous low flow years between 2003 and 2009 and (b) during the continuous high flow years between 2010 and 2016. The bathymetric data were collected from ZSIEC.

2.2. Field Data and Analysis

Because of the fine sediment that can be easily resuspended from the seabed by tidal currents or river flows, the bed elevation in QE has been adjusting drastically on the interannual and seasonal time scales. The extent of bed erosion and deposition in 1 year can be more than 5 m [*Chien et al*., 1964]. Owing to the importance of the morphological evolution of the large inside bar for flood protection, navigation, saline water intrusion, etc., the bathymetry of the estuarine reach of QE has been measured routinely in every April and July (representing before and after flood seasons, respectively) since 1981.

Figure 3 shows the laterally averaged longitudinal profile of the estuarine reach in April and July over years of 2003–2009 and 2010–2016. The former period is continuous low flow years, with the annual discharge between 374 and 717 m^3/s, whereas the latter is continuous high flow years, with the annual discharge between 845 and 1390 m^3/s (Figure 2a). The average discharges before April and July of the two periods are 534 and 856 m^3/s and 943 and 1799 m^3/s, respectively. During the two periods, the elevations of the inside bar in July were lower by about 0.4 and 0.8 m than in April, respectively. The elevation in the latter period was lower by about 1.0 m than in the former period. Meanwhile, about 80 km downstream from Zakou, the bed level in July was higher by about 0.2 m and 0.3 m than in April in the two periods, respectively. This indicates that there is a sediment exchange between the upstream and downstream. Overall, the upper part of the bar is characterized by erosion during flood seasons or high flow years or accretion during dry seasons or low flow years. In contrast, the lower part of the bar has the opposite trends.

3. Model Description

We model the inside bar formation and evolution using Delft3D. It is a process-based morphodynamic model which has been widely used for various time scale and spatial-scale hydrodynamics and morphodynamics in

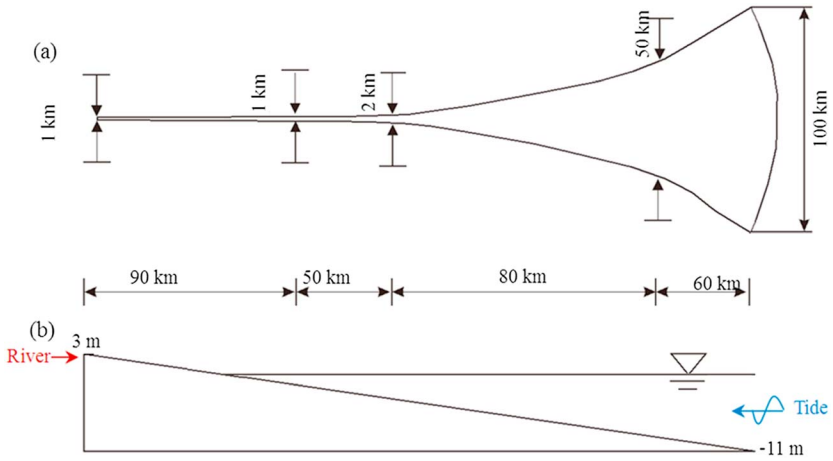

Figure 4. Sketch of the modeled estuary. (a) Geometry (top view) and (b) initial bathymetry (side view).

coastal and estuarine environments [e.g., *Wang et al.*, 1995; *Hibma et al.*, 2003; *van der Wegen and Roelvink*, 2008; *Zhou et al.*, 2014, 2017].

3.1. Model Geometry

Compared to the complex models that contain the state-of-the-art physical descriptions and parameterizations, idealized models focus on the first physical principles and isolate and analyze the prevailing morphological processes, through input reductions including simplified geometry and boundary conditions and formulations. In recent years, idealized models have been widely applied in the studies on the physical processes and underlying mechanisms in estuarine environments [e.g., *Hibma et al.*, 2003; *van der Wegen and Roelvink*, 2008; *Nardin et al.*, 2013; *Zhou et al.*, 2014; *Bolla Pittaluga et al.*, 2015].

Because QE is a very shallow and vertically well mixed estuary [*Su and Wang*, 1989; *ECCHE*, 1992; *Xie et al.*, 2017], the depth-averaged transport equations neglecting mixing processes can be used for most modeling purposes. An idealized horizontal 2-D model is constructed by a 280 km long basin with width varying from 1 km (from the landward end to km 90) to 100 km exponentially, mimicking the present QE outline but the continuous bends at the upper parts are straightened to exclude the secondary flow induced by the curvature effects (Figure 4).

The estuary is arranged in the west-east direction and symmetrical to the axis line. The initial bed level decreases linearly from 3 to −11 m from the landward end to seaward end, with mean sea level as datum. This implies a uniform initial bed slope of 5×10^{-5}. A curvilinear grid is used, with the minimum grid size of only 50 m located at the upstream end and relatively lower resolution in the lower estuary (grid size of 1000–5000 m). A 60 s time step is used.

3.2. Hydrodynamics and Sediment Transport

Flow is calculated based on the horizontal 2-D shallow water equations (see *Deltares* [2014] for details). Transport of the suspended sediment is based on the advection-diffusion equation, in which the erosion/deposition fluxes between the bed and the water column are calculated with the well-known Krone-Partheniades formulation [*Partheniades*, 1965]:

$$\begin{aligned} E &= M\left(\frac{\tau}{\tau_{ce}} - 1\right), \tau > \tau_{ce} \\ D &= w_s c\left(1 - \frac{\tau}{\tau_{cd}}\right), \tau < \tau_{cd} \end{aligned} \tag{1}$$

where E and D are erosion and deposition fluxes (kg/m^2/s), M is erosion parameter (kg/m^2/s), τ is bed shear stress (N/m^2), τ_{ce} and τ_{cd} are critical erosion and deposition shear stresses (N/m^2), and w_s is the settling velocity (m/s). The erosion parameter (M) is 2.0×10^{-5} kg/m^2/s, following suggestions by *Winterwerp and van Kesteren* [2004]. τ_{ce} and τ_{cd} are related to several factors such as sediment grain size, flocculation, and consolidation [e.g., *Mehta et al.*, 1989]. In QE, no field or laboratory data were reported for the critical

Table 1. The Values of the Model Parameters

Parameter	Symbol	Value
Manning coefficient	n	Around 0.012
Settling velocity	ω_s	0.5 mm/s
Specific density for cohesive sediment	ρ_w	2650 kg/m^3
Dry bed density	ρ_s	500 kg/m^3
Horizontal eddy viscosity	υ_H	1 m^2/s
Critical erosion stress	$\tau_{cr,e}$	0.15 N/m^2
Critical deposition stress	$\tau_{cr,d}$	0.15 N/m^2
Erosion rate	M	2.0×10^{-5} kg/m^2/s
Cell size	Δx, Δy	50–5000 m with spatial variations
Time step	Δt	60 s
Morphological scale factor	M_F	1

erosion/deposition shear stresses. Herein, both are defined to be around 0.15 N/m^2, consistent with previous numerical models of Hangzhou Bay by *Xie et al*. [2009, 2013]. w_s in QE varies between 0.1 and 3 mm/s [*Han et al*., 2003] and is set to be 0.5 mm/s in the model. Sensitivity analysis showed that given the different but reasonable values for these parameters, the inside bar and the dextral morphology could be formed, with some minor differences of the inside bar shapes and the corresponding time scales.

For the reference run, at the landward boundary a constant discharge of 1000 m^3/s is prescribed. This value is close to the annually averaged river discharge in QE. The suspended sediment concentration (SSC) is set to be 0 kg/m^3, denoting that there is not sediment supply from the Qiantang River. M_2 constituent is the dominant tidal component in the Hangzhou Bay [*ECCHE*, 1992]. Moreover, for QE the tidal asymmetry generated within the estuary is much more important (indicated by the formation of the tidal bore) than the tidal asymmetry from the open sea. At the seaward boundary, the model is forced by a semidiurnal M_2 tide with tidal amplitude of 2 m, neglecting the other constituents. Sensitivity analysis showed that with the mean observed tidal amplitude of QE (around 1.5 m), the downslope of the modeled inside bar profile was steeper than the measured, as will be shown later. An averaged SSC of 1.0 kg/m^3 is prescribed, close to the annual average SSC at the mouth [*ECCHE et al*., 1992; *Xie et al*., 2017]. Moreover, the so-called "Thatcher-Harleman" condition at this boundary is employed to prevent sudden SSC variations at the turning of the tide [*Van der Wegen et al*., 2016]. Wind waves are excluded in the present study.

3.3. Bed Level Changes

The elevation of the bed is dynamically updated at each computational time step, based on the conservation of sediment mass. For long-term morphodynamic models, the morphological scale factor M_F is often applied to reduce the computing time. Our preliminary runs showed that the inside bar morphology in the present study can be reproduced at a temporal scale of several years, within an acceptable computational time. In addition, when using the MF approach for the seasonally varying river discharges, the hydrograph compression that squeezes a yearly hydrograph to a short period should be taken into account [*Guo et al*., 2015]. For simplification, the bed level change in this study is updated by a M_F of 1.

The model input parameters in this study are listed in Table 1.

3.4. Model Runs for Sensitivity Analysis

As the first step, the Coriolis force is excluded by assuming the latitude of the estuary to be 0°, so that we can focus on the physical processes forced by the river and tides. As aforementioned, the reference run is forced by a constant river discharge of 1000 m^3/s and the M_2 tide of 2 m amplitude. Then two runs with constant discharges of 500 and 1500 m^3/s are carried out, keeping all the other input conditions invariant. The discharges 500, 1000, and 1500 m^3/s represent the annual river flow in the low, intermediate, and high flow years, respectively (Table 2).

To estimate the influence of seasonal discharge changes and estimate the dominant discharge that is responsible for the sediment accumulation (known as bed formation discharge), another case is considered, starting with the same initial bathymetry and running for a duration of 3 years, but the monthly varying discharges in QE (as shown in Figure 2b) is prescribed at the landward boundary. Preliminary results showed that such a series of discharge is not large enough to invert the bed aggradation in low flow season to degradation,

Table 2. Overview of Model Input Variations in the Sensitivity Analysis

Group	River Discharge	Amplitude of M_2	Critical Shear Stresses	Initial Bathymetry	Coriolis	Model Duration
1	500, 1000, and 1500 m^3/s and monthly averaged	2 m	0.15 N/m^2	3 to −11 m, linearly	off	3 years
2	daily variation	2 m	0.15 N/m^2	Bathymetry at the inside bar formation in the reference case	off	1 year
3	1000 m^3/s	1, 1.5, and 2 m	0.15 N/m^2	3 to −11 m, linearly	off	3–10 years
4	1000 m^3/s	2 m	0.15, 0.25, and 0.35 N/m^2	3 to −11 m, linearly	off	3–11 years
5	1000 m^3/s	2 m	0.15 N/m^2	3 to −11 m, linearly	on (30.5°N and 30.5°S)	3 years

because the flood peak is smoothed by monthly averaging. Hence, an additional run is designed to prescribe the landward boundary conditions using the daily discharge according to the time series of daily discharges of QE in a representative intermediate flow year, in which the maximum is larger than 10,000 m^3/s. The first 5 months are set as high flow season, and the following 7 months are set as low flow season.

Next, the influence of tidal amplitude is investigated, by varying tidal amplitude at the seaward boundary to be 1 m and 1.5 m, respectively. QE is characterized by the high SSC, which is probably responsible for the drastic bed evolution of the estuary [e.g., *Pan and Huang*, 2010]. To see the effect of different SSC on the inside bar morphology, two larger critical shear stresses for deposition and erosion, 0.25 and 0.35 N/m^2, are set to obtain lower SSC in the estuary. These simulations are ceased if the inside bar generated reaches the comparable height as that in the reference run.

Then, the latitude of the estuary is set to be 30.5°N and 30.5°S, to assess the influence of the Coriolis force in the Northern and Southern Hemispheres. The 30.5°N is the real latitude of QE. All the other input conditions are identical to the reference run.

4. Model Results

4.1. Morphological Evolution Processes

Figures 5 and 6 illustrate the bed evolution. The large inside bar morphology can be generated within a period of 36 months. Sediment accumulates at the middle reach, between the 75 and 175 km sections, with the bar top being located at around 125 km. The bed level at the top increased from −3 m to 1.35 m, with

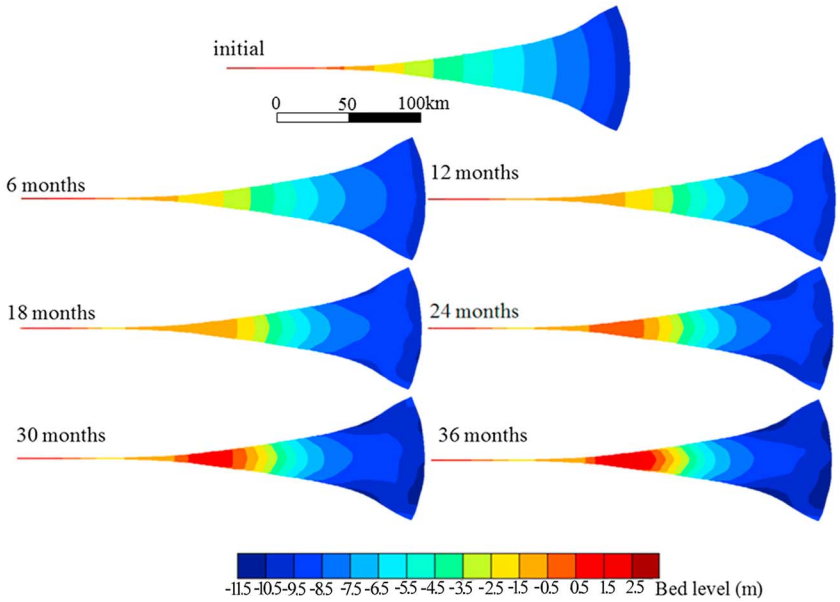

Figure 5. Inside bar evolution without taking into account the Coriolis force.

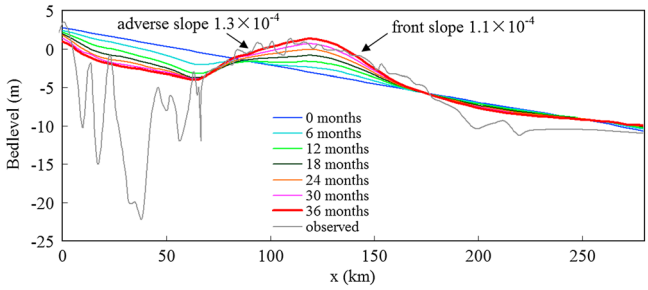

Figure 6. Evolution of the longitudinal profile of the inside bar morphology. The gray line indicates the real profile.

rates of about 0.1 m per month. At the upper reach, $x < 75$ km, the bed was continuously eroding, while the lower reach downstream of 175 km has a trend to evolve toward a subaqueous plain. The front and adverse slopes of the simulated inside bar are 1.1×10^{-4} and 1.3×10^{-4}, respectively, in good agreement with the reality. It should be noted that the depth at the upper reach is much less than the real situation. The real depth (up to 20 m) is probably related to the erosion by high flow discharge and will be discussed later. With the inside bar formation, two tidal channels have been developed at the northern and southern banks of the lower estuary. The lengths and widths of the channels are 15.6 km and 6 km, respectively, and the maximum depths are around 12 m.

A longer-term simulation (up to 10 years) shows that the inside bar can grow continuously. A central shoal was gradually developed around the bar top. Meanwhile, side channels were gradually developed and became the main passages for tidal currents. Although this pattern is reasonable numerically, it completely deviates from reality. Therefore, if the model is merely forced by tides and low river discharge, with unlimited sediment supply, the inside bar will grow continuously to become much larger than in reality. However, the actual growth will be constrained by erosion from high flow discharges, as will be shown below.

4.2. Temporal Changes of Hydrodynamics and Sediment Transport

Figure 7 illustrates the changes of hydrodynamics and sediment transport along the estuary at the initial state and at the bar formation after 3 years. At the initial state, both the high and low waters decrease slightly seaward (Figure 7a). After the bar is formed, the low water level is enhanced upstream of the inside bar peak, but it falls slightly in the seaward side of the peak. Correspondingly, the tidal range decreased at the upstream, with a maximum being formed downstream of the bar (Figure 7b). This agrees with the real situation as shown in Figure 1d. In the upstream part, the flood maximum was lower than the ebb maximum, revealing ebb dominance (Figures 7c and 7d). The inside bar area is flood dominated, while the mouth area is ebb dominated. After the inside bar formation, the flood-dominant area extends by about 10 km to both landward and seaward, and the peak of the ratio of the peak flood current velocity to ebb current velocity increases from 1.5 to 2. This agrees with the deduction by *Chien et al.* [1964] that the development of the large sand body in QE favors the deformation of tidal waves, causing significant tidal asymmetry.

Suspended sediment concentrations in the estuary are characterized by the obvious maxima between 100 and 150 km, up to about 9 kg/m^3 (Figure 7e). After the sandbar formation, the turbidity maximum moved downstream by about 20 km, but the peak concentration increased to be about 10 kg/m^3. In reality, the SSCs in QE are high, up to 10 kg/m^3 around Yanguan section (about 140 km from FPS). The high SSCs are to a large degree responsible for the drastic morphological evolution [*Pan and Huang*, 2010]. The input and output sediment volumes were on the order of 10^6 m^3 per tide at the mouth and decreased upward (Figures 7f and 7g). The net sediment transport has decreased gradually with the morphological evolution, from up to 0.2×10^6 m^3 to less than 0.1×10^6 m^3 (Figure 7h). The spatial gradient of residual sediment transport controls morphodynamic development. Since the gradient around the bar area is still relatively large following the inside bar formation, the system has not reached its morphological equilibrium.

4.3. Sensitivity Analysis

4.3.1. The Role of River Discharges

Figure 8a illustrates the longitudinal profiles for the cases of constant river discharges, 500, 1000, and 1500 m^3/s, and the monthly varying discharge after 3 years. For the former three cases, large discharge led

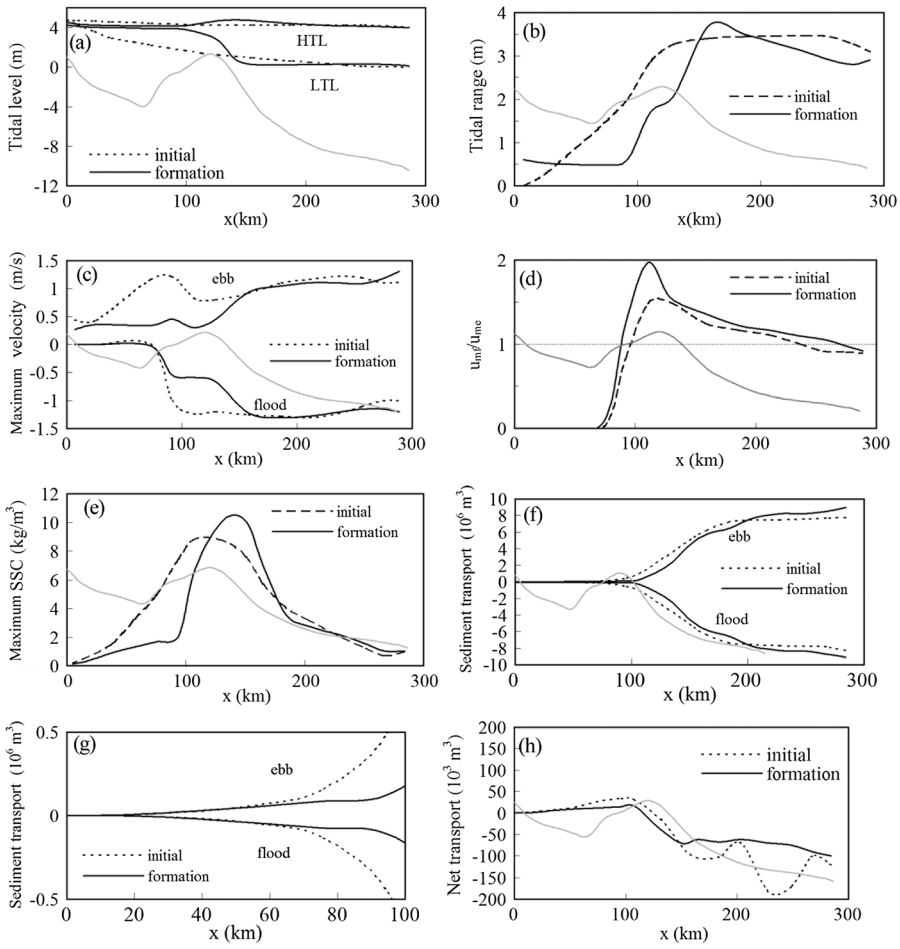

Figure 7. Hydrodynamics, sediment transports, and suspended sediment concentrations along the estuary at the initial state and after the inside bar formation. (a) High and low tidal levels (denoted by HTL and LTL), (b) tidal ranges, (c) maximum flood and ebb velocities, (d) ratio between the maximum flood velocity (u_{mf}) to maximum ebb velocity (u_{me}), (e) maximum suspended sediment concentrations, (f) cross-sectional flood and ebb sediment fluxes in one tide, (g) zoom in of x = 0–100 km in Figure 7f, and (h) the net sediment transport in one tide cycle. The gray line in the panels indicates the longitudinal bathymetry along the estuary after the sandbar formation.

to lower bed level at the upstream, due to larger erosion capacity of the river flow. Compared to the intermediate flow year, the sandbar apex was about 0.50 m higher and about 1 m lower in the low and high flow years, respectively. These results indicate thus that the extent of the bed level change between two neighboring periods of high and low flow years at the apex can be about 1.5 m, about 15% of the bar height (10 m). These values are in line with the real situation shown in Figure 3. Meanwhile, the location of the apex moved upward or downward by about 5 km in the periods of low and high flow years. The sediment exchange between the upper and lower parts in Figure 3 is reproduced well. Namely, the bed level changes at the lower part of the sandbar front slope were opposite to the upper part. The extents of the bed level change in the lower part were less than those in the upper part because the lower part is wider.

The upstream bed level in the case with the monthly varying discharge is a little higher than that of the 1000 m^3/s case. It can be estimated that the bed formation discharge of the estuary should be a little larger than 1000 m^3/s. This is consistent with *Chen et al.* [2006] based on the time series of monthly averaged discharges in QE that the bed formation discharge is about 1100 m^3/s after the construction of FPS in 1977, and it was about 1600 m^3/s before 1977. The decrease of the bed formation discharge after 1977 can be explained by the operation of the power station, which decreased the flood peaks.

The bed evolution of the sandbar can be explained by the daily cumulative sediment transport, as shown in Figure 8b. The cross sections at x = 75, 125 and 200 km can roughly represent the head, apex, and tail of the

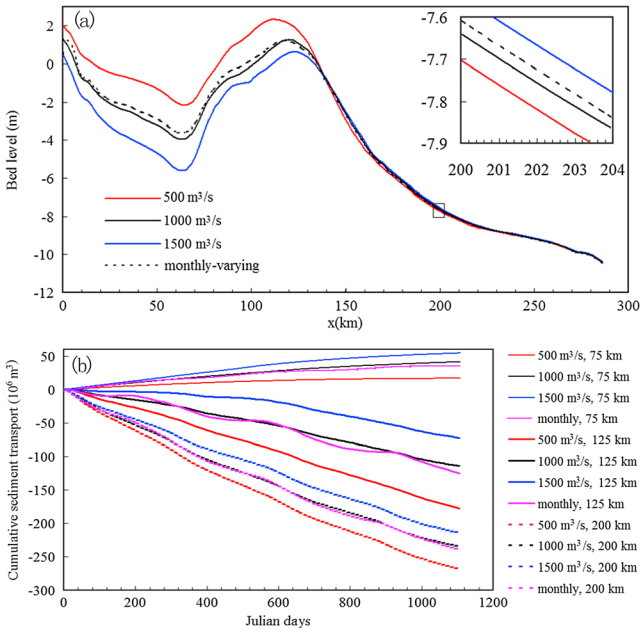

Figure 8. The (a) longitudinal profile and (b) cumulative sediment transport of the estuary at x = 75, 125, and 200 km after 3 years in the low, intermediate, high, and monthly varying flow years.

sandbar, respectively. At 75 km, the sediment transport is seaward, and the sediment flux increases with increasing discharge. At 125 and 200 km, the sediment transport is landward, and the flux decreases with increasing discharge, indicating that the larger river flow attenuated the flood currents. The sediment accretion in the adverse slope region of the sandbar (between 75 and 125 km) are 195, 157, and 128 $\times$ 10^6 m^3 over the 3 years in the 500, 1000, and 1500 cases and 92, 121, and 143 $\times$ 10^6 m^3 in the front slope region. Hence, the larger the river discharge is, the less sediment will be transported to the adverse slope region and the more sediment will be deposited in the front slope region. In the case of monthly varying discharge, the sediment transport undulates with the seasonal variation of river discharge. This is especially apparent at the upstream. However, the monthly averaged discharge was not large enough to reverse the accretion of the sandbar to erosion.

Figure 9a illustrates the bed level changes during the high and low flow seasons over 1 year in the case of daily varying discharge. During the first 5 months, the sandbar apex was eroded by 0.7 m, about 7% of the bar height. In the following 7 months of low flow, the bed level was basically recovered. The bed was continuously eroded upstream of 75 km. However, the maximum depth of about 6 m at the end of this run was still much less than the real maximum. In reality the large depth was formed by many floods during the last decades.

At 75 km, the sediment was continuously transported seaward. At 120 and 200 km, the sediment was transport seaward in the first 5 months and then landward in the following 7 months (Figure 9b). At the end of the first 5 months, the cumulative sediment transports at the three cross sections were 16, 42, and 29 $\times$ 10^6 m^3, respectively. This implies a net erosion of 26 $\times$ 10^6 m^3 at the reverse slope region and net deposition of 13 $\times$ 10^6 m^3 at the front slope region. Conversely, in the following 7 months, the reverse and front slopes were accreted and eroded, respectively. For the full year, sediment export and import at the sandbar area essentially balanced each other.

It should be pointed out that it is difficult to obtain a morphodynamic equilibrium because the tidal range increases landward and the peak appears near the apex of the sandbar (Figure 7b). This scenario is consistent with the suggestion by *Bolla Pittaluga et al.* [2015] that a necessary condition for an alluvial estuary in morphological equilibrium is that no amplification is experienced by the tidal wave propagating landward.

4.3.2. Effects of Tidal Amplitude and Suspended Sediment Concentration

Tidal amplitude is one of the major factors determining the hydrodynamic strength in estuaries. Figure 10a shows the longitudinal profiles of the estuary in the cases for various tidal amplitudes when the heights of

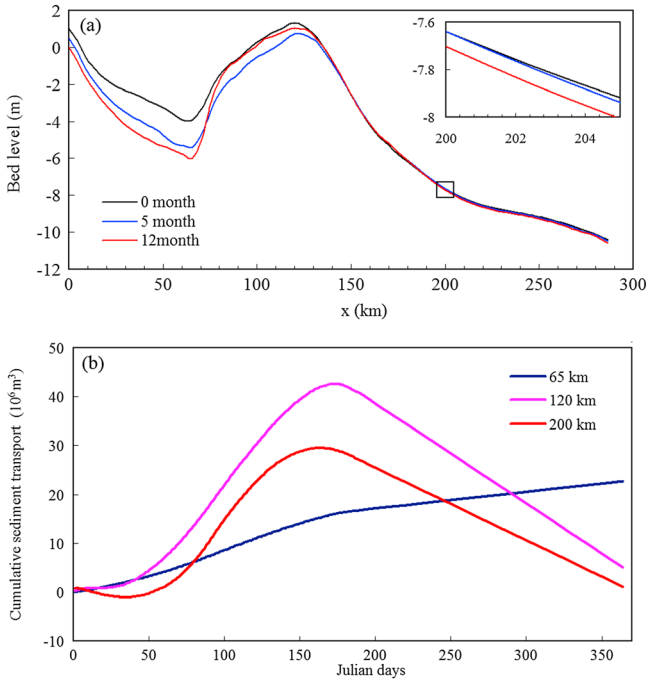

Figure 9. (a) The longitudinal profiles of the estuary in the case of daily varying discharge and (b) the cumulative sediment transport in 1 year at 75, 125, and 200 km.

the sandbar were comparable to that of the reference run after 3 years. In these cases, the sandbar can also be formed and the locations of the sandbar were comparable. The main differences for varying amplitude lay in the corresponding time scale and the front slope of the bar. A smaller amplitude led to a longer time scale and steeper front slope. The bar top in the case of 1 m amplitude moved landward by about 20 km.

The influences of the SSC magnitude were simulated by varying the critical shear stresses. The larger critical shear stresses led to lower SSC along the estuary (Figure 10b). The maximum SSC were about 9, 3.5, and 1.5 kg/m^3 for the critical shear stresses for erosion of 0.15, 0.25, and 0.35 N/m^2. For lower SSCs, the longitudinal profiles of the estuary were basically similar (Figure 10c), indicating that the shape of the sandbar is mainly determined by the large-scale hydrodynamic characteristics. The time scales for the sandbar formation of the lower SSC case were longer, because the sediment fluxes over a tidal cycle were lower. Meanwhile, the sandbar moved landward by several kilometers for larger critical stresses.

4.3.3. Coriolis Effects

Figure 11 illustrates the lateral water levels, current velocity magnitudes, and directions during flood maxima at x = 140 km and 250 km at the initial state of the three cases with different latitudes. The widths at the two cross sections are about 9 km and 50 km, respectively. The lateral distribution of the water levels and current velocities in the 0° case were north-south symmetrical. In the 30.5°N and 30.5°S cases, the water levels and tidal currents in the lower reach deviated slightly to the right-hand side and left-hand side, respectively. Taking the 30.5°N case as an example, there is a lateral water level difference of about 0.5 m at x = 250 km at maximum flood. Meanwhile, the current velocity increased and decreased slightly (less than 0.1 m/s) in the north and south banks, respectively. During ebb tide, the changes were opposite. The flow current deflected slightly to the right hand (less than 3°). Furthermore, the vectors were more restrained by the banks so that the deflections in the center were more obvious. The lateral differences of water level and current velocity decrease gradually landward. Overall, the results in the 30.5°S case were opposite to those of the 30.5°N case.

Apparent Coriolis effects on the residual sediment transport pattern at the initial state can be observed in the lower estuary (Figure 12). For the 0° case, the residual transport was directed landward from 180 to 210 km. Two circulations can be observed between 210 and 260 km, with the northern one being clockwise and the southern one being counterclockwise. For the case of 30.5°N, one larger counterclockwise circulation is observed. This gyre of residual sediment transport is consistent with the findings in previous studies that

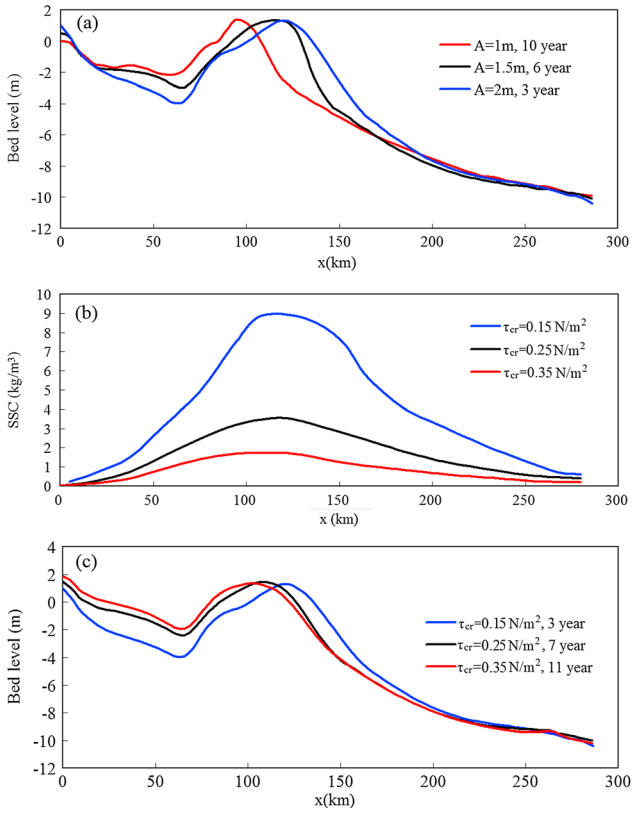

Figure 10. Effects of changes in tidal amplitude and suspended sediment concentration. (a) Longitudinal profiles under various tidal amplitudes. *A* denotes tidal amplitude at the seaward boundary. (b, c) Maximum SSCs at the initial state and the longitudinal profiles after the sandbar formation for various critical shear stresses.

water and sediment "entering in the north and leaving in the south" over one tidal cycle [*Su and Wang*, 1989; *Xie et al*., 2013, 2017]. For the case of 30.5°S (not shown in the figure), the residual sediment transport pattern is opposite to the case of 30.5°N.

Figure 13 shows the bed levels of the estuary after the 3 years modeled in the cases of 30.5°N and 30.5°S. In both cases, the sandbar was formed, and the laterally averaged bed level was consistent with the case of 0°. It is obvious that the sediment accumulation shifted southerly or northerly in the lower reach. As a consequence, a tidal flat and tidal channel were formed at the south or north, respectively. The length and width of the tidal channel is clearly larger than the channels formed in the reference run. From the residual sediment transport field shown in Figure 12, it can be confirmed that this channel is flood dominant, whereas the channels formed in the reference run are ebb dominant.

5. Discussions

5.1. Mechanisms for the Inside Bar Morphodynamics

The formation of the sandbar is related to the funnel shape of the estuary which affects the nature of the tidal wave and the characteristics of river flow and sediment conditions. Based on the observed data including annually averaged river discharge (Q_1), tidal discharge (Q_2), and sediment supply at landward and seaward boundaries, from 22 estuaries in the world, *Chien et al*. [1964] proposed that the relative location of sandbar in estuaries can be defined simply using the ratio of Q_1 and Q_2. If $Q_1/Q_2 > 0.1$, then the sandbar would be located at the mouth side; i.e., the ebb delta or mouth bar would be formed; if $Q_1/Q_2 < 0.02$, then the sandbar would be stretched deeply into the upper reach; i.e., the inside sandbar would be formed, while if the ratio is between 0.02 and 0.1, it is the transitional state. Essentially, such theory is based on the relative strengths of river flow and tidal currents. In the context of QE, the ratio is around 0.01; hence, the sandbar is stretched deeply into the middle and upper reaches of the estuary. Despite that the inside sandbar morphology is also influenced to a certain extent by sediment properties (Figure 10), the location of the sandbar is mainly determined by the large-scale hydrodynamics controlled by the combination of river discharge and tides.

The tides play the dominant role on the inside sandbar formation in estuaries. Model results in this study showed that the longitudinal profiles of the sandbar were basically similar, for all scenarios of river discharges. Tidal currents transport a large amount of sediment landward, but the small river flow cannot transport the sediment to the lower reach of the estuary. A larger tidal amplitude led to a closer match with the observed profiles, while a tidal amplitude close to the mean tidal amplitude of QE led to a steeper front slope of the sandbar. This indicates that the role of spring tides on the morphological developments is larger than the intermediate or neap tides.

Increasing river discharge leads to a larger ebb tidal volume at the same cross-sectional area and enlarges the bed shear stresses and associated sediment transport capacity [e.g., *Canestrelli et al*., 2010; *Yu et al*., 2012; *Guo et al*., 2014]. The seasonal changes of sediment transport and morphological evolution due to high flow and

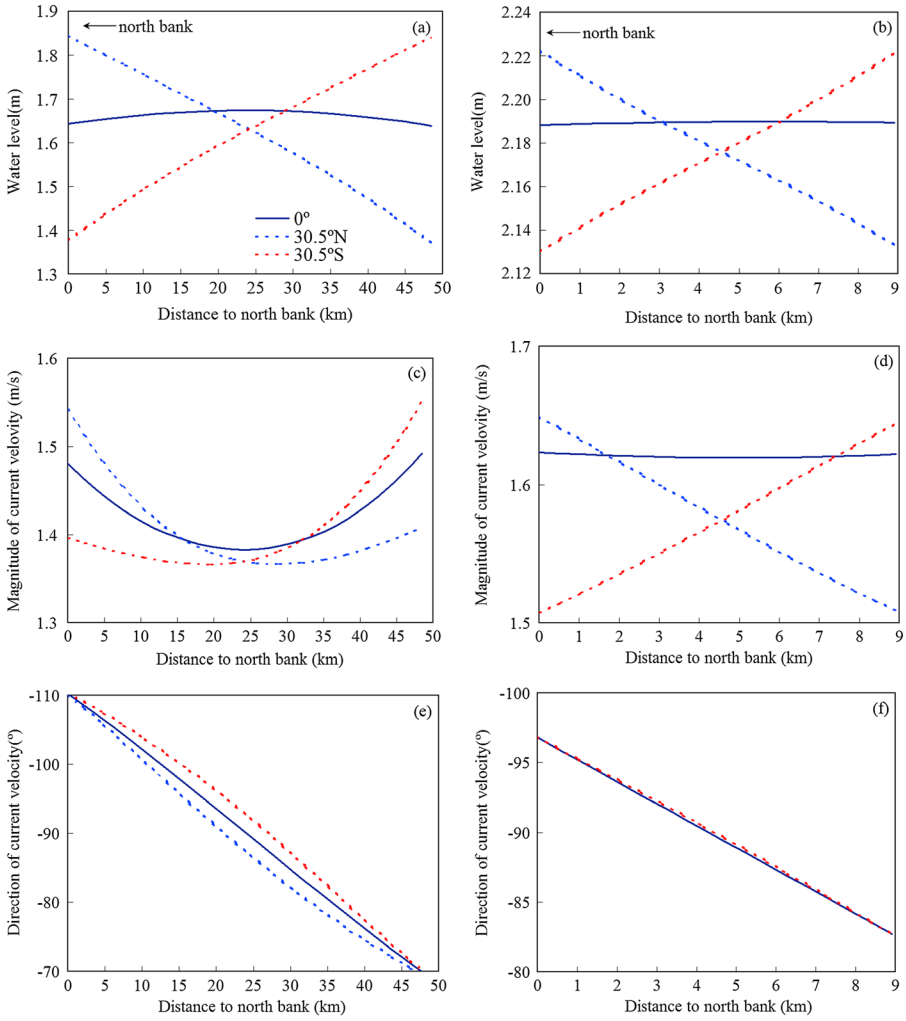

Figure 11. Lateral water levels, current velocity magnitudes, and directions at flood maxima at 140 and 250 km at the initial state of the cases of 0°, 30.5°N, and 30.5°S.

low flows have been observed in many estuaries, such as Changjiang Estuary [*Guo et al.*, 2014], Mississippi Estuary [*Shaw and Mohrig*, 2014], Mekong River [*Bravard et al.*, 2014], and Guadalquivir Estuary [*Wang et al.*, 2014]. Many estuaries with river-borne sediment supply experience deposition during high flow and are eroded during low flow. For example, the distributary channels at the Wax Lake Delta of the Mississippi

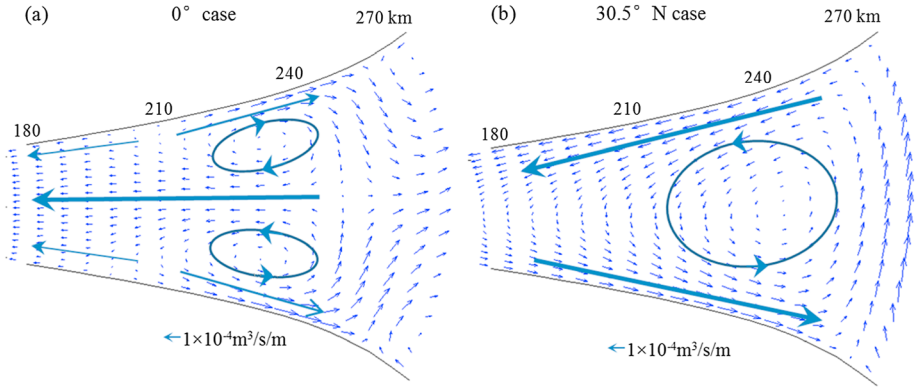

Figure 12. Residual sediment transport at initial state for the cases of (a) 0° and (b) 30.5°N.

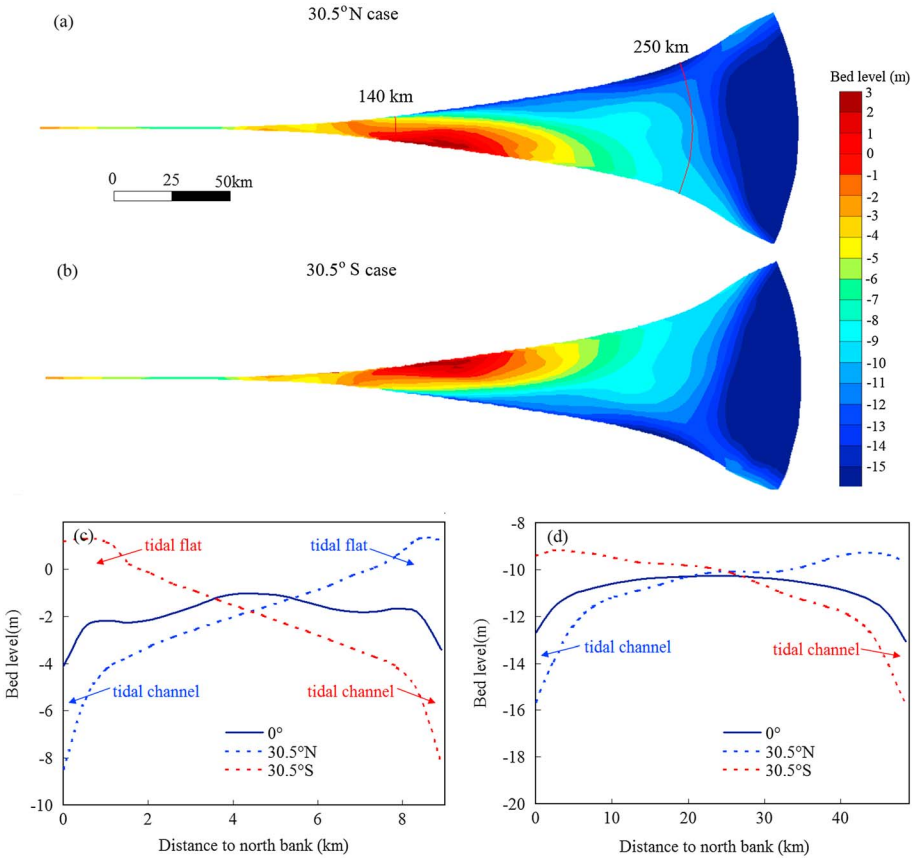

Figure 13. Bed levels of the estuary after 36 months. (a) 30.5°N case, (b) 30.5°S case, and (c, d) lateral bed levels along cross sections at 140 and 250 km, depicted in Figure 13a.

Estuary enlarged by several kilometers during high river flows with high river-borne sediment supply and retreated landward during low river flow with low sediment load [*Shaw and Mohrig*, 2014]. However, there is obvious difference for the river discharge role in QE. Riverine sediment load from Qiantang River is negligible. Therefore, the bed level changes in QE are controlled by sediment input and output at the seaside. The morphological evolution of the inside sandbar is controlled by the cycles of deposition during low discharges when the tides dominate and erosion during high discharges when the river discharge is dominant.

The temporal scale for the formation of the large inside bar is of the order of several years according to the simulations in this study. This depends on the initial conditions, imposed at the beginning of the numerical simulations [e.g., *Zhou et al*., 2014; *Bolla Pittaluga et al*., 2015]. The modeled situation mimicked the present QE. At the initial state of the simulations, the sandbar area was already floored by a large amount of sediment. In reality, the width of the upper and middle reaches of QE in the past was much larger than at present. Geological survey revealed that the width of sand accumulation body of the upper and middle QE can be up to 50 km, and the thickness can be more than 100 m [*Chen et al*., 1964; *Zhang et al*., 2015]. Hence, the sediment volume for the formation of the sandbar in the model is about 2 orders less than in reality. Therefore, the modeled temporal scale does not apply for the real historical formation of the sandbar but reflects the morphological time scale of the sandbar at present: the sedimentary material required by the bar formation was supplied to the area over a long period of time, but the reworking of the material takes a considerably shorter time. This is supported by the observations and as the model results concerning the extents of the interannual and seasonal changes of the bar height to the bar height itself.

Estuarine inside sandbars exist widely throughout the world, where river inputs are limited but tidal ranges are large enough and hence the relative strength of river flow to tidal currents is small. The spatial scale and relative location of the sandbar are also related to sediment supply and sediment fractions [*Yu et al*., 2012].

Along the margin of China's continental shelf, many estuaries of mountainous rivers which have small catchments and river discharges are mainly floored with cohesive clay or silt. The fine sediment supply mainly comes from the seaside where it has dispersed from the two large river mouth systems, i.e., the Changjiang and Yellow Rivers [*Gao and Collins*, 2014; *Gao et al*., 2016]. The results in this study are relevant for similar estuaries.

5.2. Dynamic Equilibrium of the Sandbar

One of the most important concepts associated with the estuarine morphodynamics is the equilibrium status [*Zhou et al*., 2017]. In general, equilibrium in an estuary is reached when the net sediment transport in a tidal cycle is constant throughout the estuary [e.g., *Friedrichs and Aubrey*, 1996; *Lanzoni and Seminara*, 2002; *Van der Wegen and Roelvink*, 2008; *Bolla Pittaluga et al*., 2015]. However, such a static equilibrium rarely exists on actual or modeled coastal environment. Hence, *Friedrichs* [2011] further proposed the dynamic equilibrium concept for tidal flat based on the analytical solution. It elucidates that observed tidal morphology approximates a dynamic equilibrium over annual or longer time scales. On a shorter time scale, the morphology may deviate from the dynamic equilibrium and approach one or the other extreme depending on the prevailing forcing condition. The dynamic equilibrium theory was embedded for the DET-ESTMORF (dynamic equilibrium theory-ESTMORF) model by *Hu et al*. [2015] and showed good model performance in both long-term and short-term morphodynamic predictions. This concept can also be applied to estuaries. In QE, river discharge and tidal currents play distinct roles. In the season or years with low river discharge, the tidal flow is dominant, and sediment is transported landward. As a result, the sandbar is accreted and the top part moves landward. In contrast, when the high river discharge is prevailing, sediment is transported seaward, and the bar is eroding and the top moves seaward (Figure 8). On a multiyear scale, the dynamic equilibrium can be maintained.

Bed formation discharge determines the quasi-equilibrium morphology of an alluvial channel [e.g., *Lanzoni et al*., 2014]. When the river discharge is lower or higher than the bed formation discharge, the bed tends to be aggraded or degraded. *Lanzoni et al*. [2014] found that the bed formation discharge in the intermediate reach of the Po River, Italy, is quite close to the mean yearly discharge. Although they considered a river-dominated case and we deal with a strong tide-influenced case, the bed formation discharge in QE was also found to be close to the mean yearly discharge. The bed formation discharge of the alluvial estuary estimated by means of morphodynamic model was consistent with the results based on the field data.

5.3. Mechanisms for the Estuarine Dextral Morphological Patterns

Movements of water and sediment particles in all coastal and estuarine environments are ubiquitously influenced by Coriolis forces, due to the rotation of the Earth [e.g., *Schramkowski and de Swart*, 2002; *Van der Vegt*, 2006; *Li et al*., 2011]. Due to the Coriolis effects, the flow and sediment motions lean to right-hand side of the estuary (looking seaward). As a result, the water is shoved to right-hand bank (dextral diversion), and subsequently, water level difference between the right and left banks is caused. *Jin and Shen* [1993] proposed the analytical solution of the transversal water level difference caused by the Coriolis forces:

$$\Delta \mathrm{H} = \frac{BUf}{g} \tag{2}$$

where ΔH is the transversal water level difference, B is the width of the estuary, U is the flow velocity, $f = 2\omega \sin\varphi$ is the Coriolis parameter, in which ω is the angle velocity of the Earth rotation, φ is the latitude, and g is the gravity acceleration. Because ω and g are constants of 7.27×10^{-5} rad/s and 9.8 m/s^2,

$$\Delta \mathrm{H} = 1.484 \times 10^{-5} BU \sin\varphi \tag{3}$$

It can be seen from equation (3) that the transversal water level difference induced by Coriolis force is related to the cross-sectional width, current velocity, and the latitude of the estuary. For our case, using the maximum flow velocity of 1.4 m/s and the width of 50 km at x = 250 km and the latitude of 30.5°, the water level difference between the two banks of the QE is 0.52 m, close to the modeled results, as shown in Figure 11a.

The other Coriolis effects corresponding to the water level difference are (1) the large-scale counterclockwise or clockwise circulation of water flow, (2) the residual sediment transport circulation, and (3) the gradual

development of the dextral morphological patterns, as shown in Figures 12 and 13. *Schramkowski and de Swart* [2002] suggested that at smaller scale (the thresholds is up to a kilometer), the Coriolis effects will not be important. This explains the indiscernible changes of hydrodynamics and morphological development in the upper part of the estuary.

For large and mesoscale oceanic processes, the external and internal Rossby radius of deformation are emerging as important quantities in determining horizontal scales [e.g., *Gill*, 1982; *Emery et al*., 1984; *Fennel et al*., 1991]. The external Rossby radius (R_e) is the length scale for barotropic phenomena, over which the gravitational tendency to flatten the free surface is balanced by the tendency of the Coriolis acceleration to deform the surface. It can be calculated as follows:

$$R_e = \frac{\sqrt{gH}}{f} \tag{4}$$

where H is the water depth. In estuarine environments, H is normally on the order of 10^1 m; hence, R_e is on the order of 10^2 km. This is in the same order of magnitude as the width at the mouth of the estuary, indicating that the Coriolis effect is indeed important, explaining the single-cell circulation caused by the Coriolis effect. The internal Rossby radius, the length scale for baroclinic phenomena, depends on the vertical stratification, thus scaling internal motions in their adjustment to geostrophy. Because QE is very well mixed, the effect of vertical density differences is very small. In this study, we used a horizontal 2-D model, because of the lack of stratification. Subsequently, there was simply no internal wave.

The associated dimensionless parameter, the inverse Rossby number (${R_0}^{-1}$), can be used to characterize the importance of Coriolis force [*Van der Vegt*, 2006]:

$${R_0}^{-1} = \frac{fB}{U} \tag{5}$$

Using the maximum current velocities and widths at x = 250, 140, and 90 km, ${R_0}^{-1}$ are 2.6, 0.4, and 0.04, respectively. At the lower estuary, the influence of the Coriolis force is larger than the inertia, while at far upstream the influence is negligible.

Many tidal channels in estuarine environments provide natural accesses to harbors and intakes and outfalls for power plants, which gives them economic value. It is shown in this study that Coriolis effects can modify the behavior of flood and ebb-dominated tidal channels. Without the Coriolis force, a double-ebb-channel system is formed at the north and south banks. With the Coriolis force, however, a single-flood-channel system is formed. It is notable that the tidal channel system in the present study is different from those in narrow and long estuaries. One well-known example of the latter is the Western Scheldt estuary in the Netherlands [*Van Veen*, 1950; *Hibma et al*., 2003; *Van der Wegen and Roelvink*, 2008]. This 160 km long funnel-shaped estuary, with an entrance (Vlissingen) width of 5 km, exhibits a well-developed system of channels and shoals, in which a single meandering ebb-dominated channel was separated by shoals from the flood-dominated side channels. The notable difference of tidal channel and sandbar developments in the lower QE and the Westerschelde estuary should be probably attributed to the difference in convergence or in the availability of sediment. As a matter of fact, the lower QE is more comparable to the mouth area (downstream of Vlissingen) where the system of channels and shoal is much less well developed. A previous study by *Xie et al*. [2009] using a morphodynamic model with the real land boundaries and baythymetry of Hangzhou Bay revealed that the formation of northern tidal channel is related to the spatial gradients of flood dominance. Although there are probably other factors like the propagation direction of tidal wave from the seaside and headland along the north bank, Coriolis effects play one of the most important roles for the channel formation in Hangzhou Bay. In narrow and long estuaries, Coriolis effects are relatively weak, but in wide and convergent estuaries, Coriolis effects play an important role in the channel-shoal system.

The role of Coriolis force on the short-term current velocities is small (normally less than 0.1 m/s); however, on a longer time scale, Coriolis effects have a profound impact on the morphological feature of the estuary. Furthermore, with respect to coastal engineering works like seawall protection, channel training, and sand extraction, the Coriolis effects are of major practical importance. The right- or left-hand bank of the estuary could suffer a larger risk of erosion by the currents.

5.4. Model Limitations

In order to make the model as transparent as possible, we have limited ourselves to some of the major physical processes of the estuary and we have neglected other processes that may play important roles under certain circumstances.

1. The effect of estuary curvatures has been disregarded due to the schematized geometry. The concave and convex banks are normally characterized by relatively larger and smaller current velocities and water depths, respectively, due to centrifugal force. This is especially apparent at the upstream part from Ganpu of QE.
2. Waves were excluded in the model. Locally generated wind waves can enhance the resuspension of bottom sediments and result in erosion on the shallow bed, particularly the front slopes and the top part of the inside bar. Nearshore waves (e.g., swells and storm waves) can induce alongshore sediment drift and tend to inhibit the growth of sandbar.
3. The effects of salinity and density gradients were not accounted for.
4. Processes of sediment sorting and sand-mud interactions also deserve attention. The present model assumed that the estuary was floored with uniform cohesive sediments and did not include any sand fractions. For mud transport, there is no downslope effect. The bed load transport of sandy sediments could be important to stabilize the bed [e.g., *Van Rijn*, 1993].
5. The seaward boundary was forced by M_2 constituent, and other constituents were neglected. In particular, the amplitude and phase of the external overtide M_4 can modify the tidal asymmetry and subsequently influence the geomorphological development in the estuary to a certain extent [e.g., *Lanzoni and Seminara*, 1998; *Schramkowski and de Swart*, 2002; *Wang et al*., 2002].

Despite the assumptions made in this study, the model generally shows its capability to simulate the morphological evolution of the large inside sandbar system in a reasonable manner, which is qualitatively in agreement with natural systems.

6. Conclusions

In this study, the morphodynamic behavior of inside sandbar and the dextral morphology in convergent estuaries has been investigated, based on an idealized morphodynamic model. The model represents an idealized wide, shallow basin with river and tidal forces comparable to the present QE. The sandbar was reproduced first, and then sensitivity analysis of annual and seasonal variations of river discharges and Coriolis effects were carried out.

The relative strengths of river flow and tidal currents are responsible for the location of the sediment accumulation. The formation of the inside sandbar in estuaries is mainly caused by landward sediment transport from the lower reach. The high suspended sediment concentration in the estuary is responsible for the drastic bed level changes. The local tidal range and flood dominance were enhanced with the accretion. During interannual and seasonal high and low flow cycles, the inside bar was subjected to erosion and accretion and the bar top shifts landward and seaward repeatedly. The magnitude of the bed level changes can be up to 15% of the bar height. Meanwhile, sediment exchanges occur between the upstream and downstream parts of the bar. The sediment flux at the seaward end of the bar is basically balanced during the high and low river flow seasons over 1 year. In addition, the bed formation discharge was estimated to be close to the annual mean discharge.

Coriolis force controls the development of dextral morphological patterns in the estuary. It results in the lateral water level difference and subsequently gives rise to a large-scale gyre of residual sediment transport. In the Northern Hemisphere, the water level is higher at the right-hand bank, and the gyre is counterclockwise. As a result, the seaward end of the inside bar shifts to the right-hand bank. The role of Coriolis force is opposite to those in the Southern Hemisphere. Coriolis effects also modify the behavior of flood and ebb tidal channels.

Acknowledgments
This research was supported by the National Natural Science Foundation of China (grant 41676085) and Zhejiang Provincial Natural Science Foundation of China (grant LY16D060004). We wish to thank John B. Shaw, Maarten van der Vegt, two anonymous reviewers, the Associate Editor, and the Editor for their constructive comments to improve this work greatly. We also thank Stuart Pearson from Delft University of Technology for checking the manuscript. Bathymetric data in Figures 1 and 3 were provided by Zhejiang Surveying Institute of Estuary and Coast, China (ZSIEC). River discharge data in Figure 2 were provided by Hydrology Bureau of Zhejiang Province, China (HBZPC). We note that there are no data sharing issues since all of the numerical information is provided in the figures in the paper.

References

Bolla Pittaluga, M., N. Tambroni, A. Canestrelli, R. Slingerland, S. Lanzoni, and G. Seminara (2015), Where river and tide meet: The morphodynamic equilibrium of alluvial estuaries, *J. Geophys. Res. Earth Surf.*, *120*, 75–94, doi:10.1002/2014JF003233.

Bravard, J. P., M. Goichot, and H. Tronchere (2014), An assessment of sediment-transport processes in the Lower Mekong River based on deposit grain sizes, the CM technique and flow-energy data, *Geomorphology*, *207*, 174–189, doi:10.1016/j.geomorph.2013.11.004.

Canestrelli, A., S. Fagherazzi, A. Defina, and S. Lanzoni (2010), Tidal hydrodynamics and erosional power in the Fly River delta, Papua New Guinea, *J. Geophys. Res.*, *115*, F04033, doi:10.1029/2009JF001355.

Carter, B., and C. D. Woodroffe (1994), *Coastal Evolution: Late Quaternary Shoreline Morphodynamics*, Cambridge Univ. Press, Cambridge.

Chen, J. Y., C. Z. Liu, C. L. Zhang, and H. J. Walker (1990), Geomorphological development and sedimentation in Qiantang Estuary and Hangzhou Bay, *J. Coastal Res.*, *6*(3), 559–572.

Chen, J. Y., Z. D. Luo, D. C. Chen, H. G. Xu, and P. N. Qiao (1964), The formation and historical evolution of the sandbar in Qiantang estuary [in Chinese], *Acta Geograph. Sin.*, *30*(2), 109–113.

Chen, J. Y., H. T. Shen, and C. X. Yun (1988), *Processes of Dynamics and Geomophology of the Yangtze Estuary* [in Chinese], Shanghai Sci. Tech. Pub., Shanghai.

Chen, S. M., Z. C. Han, and G. J. Hu (2006), Impact of human activities on the river reach in the Qiantang Estuary [in Chinese with English abstract], *J. Sediment. Res.*, *4*, 61–67, doi:10.16239/j.cnki.0468-155x.2006.04.010.

Chien, N., H. S. Sie, C. T. Chow, and Q. P. Lee (1964), The fluvial processes of the big sand bar inside the Chien Tang Chiang Estuary [in Chinese with English abstract], *Acta Geograph. Sin.*, *30*(2), 124–142.

Cooper, J. A. G. (1993), Sedimentation in a river dominated estuary, *Sedimentology*, *40*, 979–1017, doi:10.1111/j.1365-3091.1993.tb01372.x.

Dalrymple, R. W., R. J. Knight, B. A. Zaitlin, and G. V. Middleton (1990), Dynamics and facies model of a macrotidal sand-bar complex, Cobequid Bay—Salmon River Estuary (Bay of Fundy), *Sedimentology*, *37*, 577–612, doi:10.1111/j.1365-3091.1990.tb00624.x.

Deltares (2014), Delft3D flow user manual. [Available at http://oss.deltares.nl/web/delft3d/ manuals.]

Dyer, K. R. (1986), *Coastal and Estuarine Sediment Dynamics*, Wiley, London.

Editorial Committee for Chinese Harbors and Embayments (ECCHE) (1992), *Chinese Harbours and Embayments (Part V)* [in Chinese], China Ocean Press, Beijing.

Emery, W. J., W. G. Lee, and L. Magaard (1984), Geographic and seasonal distributions of Brunt-Väisälä frequency and Rossby radii in the North Pacific and North Atlantic, *J. Phys. Oceanogr.*, *14*, 294–317.

Fan, D. D., J. B. Tu, S. Shang, and G. F. Cai (2014), Characteristics of tidal-bore deposits and facies associations in the Qiantang Estuary, China, *Mar. Geol.*, *348*, 1–14, doi:10.1016/j.margeo.2013.11.012.

Fennel, W., T. Seifert, and B. Kayser (1991), Rossby radii and phase speeds in the Baltic Sea, *Cont. Shelf Res.*, *11*(1), 23–36, doi:10.1016/0278-4343(91)90032-2.

Friedrichs, C. T. (2011), Tidal flat morphodynamics: A synthesis, in *Treatise on Estuarine and Coastal Science*, edited by E. Wolanski and D. McLusky, pp. 137–170, Academic Press, Waltham, Mass.

Friedrichs, C. T., and D. G. Aubrey (1996), Uniform bottom shear stress and equilibrium hyposometry of intertidal flats, in *Coastal and Estuarine Studies*, edited by C. Pattiaratchi, pp. 405–429, AGU, Washington, D. C.

Gao, S., and M. B. Collins (2014), Holocene sedimentary systems on continental shelves, *Mar. Geol.*, *352*, 268–294, doi:10.1016/j.margeo.2014.03.021.

Gao, S., D. D. Wang, Y. Yang, L. Zhou, Y. Y. Zhao, W. H. Gao, Z. C. Han, Q. Yu, and G. C. Li (2016), Holocene sedimentary systems on a broad continental shelf with abundant river input: Process–product relationships, in *River-Dominated Shelf Sediments of East Asian Seas*, edited by P. D. Clift et al., *Geol. Soc. London, Spec. Publ., 429*, 231–268, doi:10.1144/SP429.4.

Geleynse, N., J. E. A. Storms, D. J. R. Walstra, H. R. A. Jagers, Z. B. Wang, and M. J. F. Stive (2011), Controls on river delta formation: Insights from numerical modeling, *Earth Planet. Sci. Lett.*, *302*, 217–226, doi:10.1016/j.epsl.2010.12.013.

Gill, A. E. (1982), *Atmosphere-Ocean Dynamics*, Academic Press, Orlando, Fla.

Godin, G. (1985), Modification of river tides by the discharge, *J. Waterw. Port Coastal Ocean Eng.*, *111*(2), 257–274.

Goodbred, S. L., and S. A. Kuehl (2000), Enormous Ganges-Brahmaputra sediment discharge during strengthened early Holocene monsoon, *Geology*, *28*(12), 1083–1086, doi:10.1130/0091-7613(2000)28<1083:EGSDDS>2.0.CO;2.

Guo, L. C., M. van der Wegen, J. A. Roelvink, and Q. He (2014), The role of river flow and tidal asymmetry on 1-D estuarine morphodynamics, *J. Geophys. Res. Earth Surf.*, *119*, 2315–2334, doi:10.1002/2014JF003110.

Guo, L. C., M. van der Wegen, D. Roelvink, and Q. He (2015), Exploration of the impact of seasonal river discharge variations on long-term estuarine morphodynamic behavior, *Coastal Eng.*, *95*, 105–116, doi:10.1016/j.coastaleng.2014.10.006.

Han, Z. C., Z. H. Dai, and G. B. Li (2003), *Regulation and Exploitation of Qiantang Estuary* [in Chinese], China Water Power Press, Beijing.

Harris, P. T. (1988), Large scale bedforms as indicators of mutually evasive sand transport and the sequential infilling of wide-mouthed estuaries, *Sediment. Geol.*, *57*, 273–298.

Hibma, A., H. J. de Vriend, and M. J. F. Stive (2003), Numerical modelling of shoal pattern formation in well-mixed elongated estuaries, *Estuarine Coastal Shelf Sci.*, *57*, 981–991, doi:10.1016/S0272-7714(03)00004-0.

Hu, Z., Z. B. Wang, T. J. Zitman, M. J. F. Stive, and T. J. Bouma (2015), Predicting long-term and short-term tidal flat morphodynamics using a dynamic equilibrium theory, *J. Geophys. Res. Earth Surf.*, *120*, 1803–1823, doi:10.1002/2015JF003486.

Huijts, H. M. K., M. H. Schuttelaars, E. H. de Swart, and T. C. Friedrichs (2009), Analytical study of the transverse distribution of along-channel and transverse residual flows in tidal estuaries, *Cont. Shelf Res.*, *29*, 89–100, doi:10.1016/j.csr.2007.09.007.

Jiang, J. Z. (1987), Discussion on Coriolis effect bring about the difference in the tidal range between two sides of Hangzhou Bay [in Chinese with English abstract], *J. Mar. Sci.*, *5*(3), 10–14.

Jin, Y. H., and H. T. Shen (1993), Effects of Coriolis' force on estuarine branch fjord [in Chinese with English abstract], *Mar. Sci.*, *4*, 52–55.

Kunte, P. D., C. Zhao, T. Osawa, and Y. Sugimori (2005), Sediment distribution study in the Gulf of Kachchh, India, from 3D hydrodynamic model simulation and satellite data, *J. Mar. Syst.*, *55*, 139–153, doi:10.1016/j.jmarsys.2004.09.008.

Lanzoni, S., and G. Seminara (1998), On tide propagation in convergent estuaries, *J. Geophys. Res.*, *103*(C13), 30,793–30,812, doi:10.1029/1998JC900015.

Lanzoni, S., and G. Seminara (2002), Long term evolution and morphodynamic equilibrium of tidal channels, *J. Geophys. Res.*, *107*(C1), 3001, doi:10.1029/2000JC000468.

Lanzoni, S., R. Luchi, and M. Bolla Pittaluga (2014), Modeling the morphodynamic equilibrium of an intermediate reach of the Po River (Italy), *Adv. Water Resour.*, *81*, 95–102, doi:10.1016/j.advwatres.2014.11.004.

Leuven, J. R. F. W., M. G. Kleinhans, S. A. H. Weisscher, and M. Van der Vegt (2016), Tidal sand bar dimensions and shapes in estuaries, *Earth Sci. Rev.*, *161*, 204–223, doi:10.1016/j.earscirev.2016.08.004.

Li, G. Y. (2007), The action of Coriolis force in evolution of the Yellow River channel [in Chinese with English abstract], *J. Hydraul. Eng.*, *38*, 1409–1413.

Li, M. T., Z. Y. Chen, D. W. Yin, J. Chen, Z. H. Wang, and Q. L. Sun (2011), Morphodynamic characteristics of the dextral diversion of the Yangtze River mouth, China: Tidal and the Coriolis Force controls, *Earth Surf. Processes Landforms*, *36*(5), 641–650, doi:10.1007/s11707-013-0418-3.

Mehta, A. J., E. J. Hayter, W. R. Parker, R. B. Krone, and A. M. Teeter (1989), Cohesive sediment transport. I: Process description, *J. Hydraul. Eng.*, *115*(8), 1076–1093.

Nardin, W., G. Mariotti, D. A. Edmonds, R. Guercio, and S. Fagherazzi (2013), Growth of river mouth bars in sheltered bays in the presence of frontal waves, *J. Geophys. Res. Earth Surf.*, *118*, 872–886, doi:10.1002/jgrf.20057.

O'Brien, M. P. (1969), Equilibrium flow areas of tidal inlets on sandy coasts, *J. Waterw. Harbors*, *95*, 43–52.

Pan, C. H., and W. R. Huang (2010), Numerical modeling of suspended sediment transport in Qiantang River: An estuary affected by tidal bore, *J. Coastal Res.*, *26*, 1123–1132, doi:10.2112/JCOASTRES-D-09-00024.1.

Partheniades, E. (1965), Erosion and deposition of cohesive soils, *J. Hydraul. Div.*, *91*(HY1), 4204.

Perillo, G. M. E. (1995), Definitions and geomorphologic classifications of estuaries, in *Geomorphology and Sedimentology of Estuaries*, 2nd ed., edited by G. M. E. Perillo, vol. 53, pp. 17–47, Elsevier Science, Amsterdam.

Savenije, H. H. G. (2005), *Salinity and Tides in Alluvial Estuaries*, Elsevier Science, Amsterdam.

Schramkowski, G. P., and H. E. de Swart (2002), Morphodynamic equilibrium in straight tidal channels: Combined effects of Coriolis force and external overtides, *J. Geophys. Res.*, *107*(C12), 3227, doi:10.1029/2000JC000693.

Shaw, J. B., and D. Mohrig (2014), The importance of erosion in distributary channel network growth, wax Lake Delta, Louisiana, USA, *Geology*, *42*(1), 31–34, doi:10.1130/G34751.1.

Su, J. L., and K. S. Wang (1989), Changjiang river plume and suspended sediment transport in Hangzhou Bay, *Cont. Shelf Res.*, *9*, 93–111, doi:10.1016/0278-4343(89)90085-X.

Van der Vegt, M. (2006), Modeling the dynamics of barrier coasts and ebb-tidal deltas, doctoral thesis, Utrecht Univ.

Van der Wegen, M., B. Jaffe, A. Foxgrover, and D. Roelvink (2016), Mudflat Morphodynamics and the Impact of Sea Level Rise in South San Francisco Bay, *Estuaries Coasts*, doi:10.1007/s12237-016-0129-6.

Van der Wegen, M., and J. A. Roelvink (2008), Long-term morphodynamic evolution of a tidal embayment using a two-dimensional, process-based model, *J. Geophys. Res.*, *113*, C03016, doi:10.1029/2006JC003983.

Van Rijn, L. C. (1993), *Principles of Sediment Transport in Rivers, Estuaries and Coastal Seas*, Aqua Pub., Amsterdam.

Van Veen, J. (1950), Ebb and flood-channel systems in The Netherlands tidal waters in Dutch, English summary, *J. R. Dutch Geogr. Soc.*, *67*, 303–325.

Wang, Z. B., T. Louters, and H. J. de Vriend (1995), Morphodynamic modelling of a tidal inlet in the Wadden Sea, *Mar. Geol.*, *126*, 289–300, doi:10.1016/S0278-4343(02)-00134-6.

Wang, Z. B., M. C. J. L. Jeuken, H. Gerritsen, H. De Vriend, and B. A. Kornman (2002), Morphology and asymmetry of the vertical tide in the Westerschelde estuary, *Cont. Shelf Res.*, *22*, 2599–2609, doi:10.1016/S0278-4343(02)00134-6.

Wang, Z. B., J. C. Winterwerp, and Q. He (2014), Interaction between suspended sediment and tidal amplification in the Guadalquivir Estuary, *Ocean Dyn.*, *64*, 1487, doi:10.1007/s10236-014-0758-x.

Winterwerp, J. C., and W. G. M. van Kesteren (2004), *Introduction to the Physics of Cohesive Sediment Dynamics in the Marine Environment*, Elsevier, Amsterdam.

Woodroffe, C. D., R. J. Nicholls, Y. Saito, Z. Chen, and S. L. Goodbred (2006), Landscape variability and the response of Asian Megadeltas to environmental change, in *Global Change and Integrated Coastal Management*, edited by N. Harvey, pp. 277–314, Springer, New York.

Xie, D. F., Z. B. Wang, S. Gao, and H. J. Vriend (2009), Modeling the tidal channel morphodynamics in a macro-tidal embayment, Hangzhou Bay, China, *Cont. Shelf Res.*, *29*, 1757–1767, doi:10.1016/j.csr.2009.03.009.

Xie, D. F., S. Gao, Z. B. Wang, and C. H. Pan (2013), Numerical modeling of tidal currents, sediment transport and morphological evolution in Hangzhou Bay, China, *Int. J. Sediment Res.*, *28*, 316–328, doi:10.1016/S1001-6279(13)60042-6.

Xie, D. F., C. H. Pan, X. G. Wu, S. Gao, and Z. B. Wang (2017), The variations of sediment transport patterns in the outer Changjiang Estuary and Hangzhou Bay over the last 30 years, *J. Geophys. Res. Oceans*, *122*, 2999–3020, doi:10.1002/2016JC012264.

Yu, Q., Y. W. Wang, S. Gao, and B. Flemming (2012), Modeling the formation of a sand bar within a large funnel-shaped, tide-dominated estuary: Qiantangjiang Estuary, China, *Mar. Geol.*, *299-302*, 63–76, doi:10.1016/j.margeo.2011.12.008.

Zhang, X., R. W. Dalrymple, S. Y. Yang, C. M. Lin, and P. Wang (2015), Provenance of Holocene sediments in the outer part of the paleo-Qiantang River estuary, China, *Mar. Geol.*, *366*, 1–15, doi:10.1016/j.margeo.2015.04.008.

Zhou, Z., G. Coco, M. Jimenez, M. Olabarrieta, M. Van der Wegen, and I. Townend (2014), Morphodynamics of river-influenced back-barrier tidal basins: The role of landscape and hydrodynamic settings, *Water Resour. Res.*, *50*, 9514–9535, doi:10.1002/2014WR015891.

Zhou, Z., et al. (2017), Is "morphodynamic equilibrium" an oxymoron?, *Earth Sci. Rev.*, *165*, 257–267, doi:10.1016/j.earscirev.2016.12.002.